Edinburgh Research Explorer

Use of Digital Image Correlation and Machine Learning for the Optimal Strain Placement in a Full Scale Composite Tidal Turbine Blade

Use of Digital Image Correlation and Machine Learning for the Optimal Strain Placement in a Full Scale Composite Tidal Turbine Blade

Jude McLoughlin, Marek J Munko, Miguel A Valdivia Camacho, Fergus Cuthill
and Sergio Lopez Dubon
School of Engineering, The University of Edinburgh
The King's Buildings, Mayfield Road
Edinburgh, Scotland
EH9 3JL
Sergio.LDubon@ed.ac.uk

Abstract

One of the challenges testing and health monitoring of large structures represents is getting as much information as possible from a specimen with a limited number of sensors. In this work, a data-driven approach was pursued to decide the optimal location of single-point strain gauges using machine learning algorithms (MLA) and information from Digital Image Correlation (DIC) measurements. The optimal strain gauge placement was computed for a range of sensor numbers and the presence of sensors in the high-gradient regions was identified. Strain maps of almost 40,000 measurements were reconstructed successfully with fewer than twenty measured values using the method employed. However, certain loss of image contrast was identified which is likely to have resulted from the treatment of non-numerical values.

1. Introduction

Nowadays, technologies such as Digital Image Correlation (DIC) allow for capturing vast information that reveals the deformation and stresses of small and large structures on almost all their surface. Compared with traditional strain gauges, it offers a huge benefit. Nevertheless, DIC requires specific setup and environmental conditions (i.e., light) that hinder their implementation outside of controlled environments (i.e., laboratories), and then the use of stain gauges is necessary. Still, the optimal number of measurement points and their location remains open. To address this, we used the information from DIC and machine learning algorithms (MLA) to select the points on a structure which are most suited for reconstructing a high-dimensional image with as few measurements as possible.

2. Literature Review

The application described in this publication relates to the full-scale test of the tidal turbine blade. The aim of this section is to investigate previous sensor placement optimisation applications and describe the contribution of the results presented in this work.

2.1 Damage Detection and Structural Health Monitoring

A wide range of studies regarding optimal sensor placement (OSP) have been concerned with damage detection and health monitoring within structures. In this regard, many of these pieces of literature investigate the optimal placement of strain sensors, with one case looking at the placement of acoustic sensors for crack detection [1]. There are applications to structures akin to the tidal turbine blade in terms of material as well as geometry, such as compressor blades [1], composite wind turbine blades [2], cylindrical composite shells [3], and composite plates [4]. Whilst these applications are similar to OSP for tidal turbine blades, none of the mentioned studies utilise DIC for reconstruction or have experimental validation from a full-scale model. Furthermore, studies for optimal sensor placement have seen applications to support structures such as trusses, in railway vehicles and bridges [5] [6], looking to improve the safety and the knowledge of required maintenance in these constructions, demonstrating the value of OSP to the civil engineering sector. Additionally, there has been investigation into the use of sensor placement optimisation for underwater structures, with the testing of a steel plate under the loads imposed by incoming waves [7], implying current interest in sensor placement for marine purposes, and the relevance of the work presented.

2.2 Structure Motion and Performance

Optimal Sensor Placement is also implemented in the monitoring of the motion of structures involved in dynamic processes, chiefly the vibrational response of assemblies undergoing periodic forces such as axial compressor casings [8], helicopter rotor blades [9], or carbon fibre laminates [10]. Most of these studies comprised the optimal placement of accelerometers [11]. The aim of these studies was to monitor the behaviour of a structure undergoing different modal vibrations which is important in cyclic processes, such as the operation of a tidal turbine, to avoid catastrophic failure when in action. The study concerning compressor casings points out the importance of this information for rotordynamic calculations and how these structures perform under realistic test conditions. A more novel study looked at the sparse placement of pressure sensors on the surface of a car in order to inform the adjustments to improve aerodynamic performance, such as the operation of a spoiler [12].

3. Test Specification and Setup

3.1 FastBlade

The experimental results were collected at FastBlade, a research facility at the University of Edinburgh. FastBlade is the first facility in the world to carry out full-scale, regenerative tests on tidal turbine blades. The testing centre allows for testing large slender structures (2-14 meters) under either static or fatigue loads, as shown in Figure 1. The facility utilises a unique Digital Displacement® Pumps system, which incorporates regenerative pumping and digital displacement hydraulics, enabling accelerated testing (up to 1Hz) with high loads (up to 1MN) [13].

The facility aims to test the mechanical response of tidal turbine structures resulting from the loads they would experience during their lifetime of subsea deployment. Thanks to cyclic loading of the specimens, it is possible to simulate years of real-world deployment in a feasible period. These accelerated tests aim to verify the design properties of the blades and, in turn, accelerate the growth of the tidal energy market.

The blade validation procedure requires collection of various kinds of data recorded along the specimen under test, including local strain, displacement, temperature and acceleration pattern. This leads to an open-ended problem of optimising sensor location to maximise the quality of information, while keeping the information bandwidth feasible by minimising the redundancy of collected data.

3.2 Digital Image Correlation

FastBlade utilises Digital Image Correlation (DIC) to record high-resolution strain and displacement information for the specimen under test. DIC is a non-intrusive optical technique which allows interpolation and generates an entire deformation field of the outer surface of any structure by tracking the movement of pixels in a camera image. The basic principle to accurately measure displacement on a flat specimen is based on dividing the image in regions or subsets of pixels. For each subset of pixels in the undeformed image a correlation function, such as the zero mean normalised sum of squared differences (ZNSSD), is used to find the subset in the deformed images:

$$C(I, I^*, u_1, v_1, u_2, v_2, n) = \frac{\frac{1}{(2n+1)^2} \sum_{i,j=-n}^{n} \prod_{t=1}^{2} \left(I_t(u_t+i, v_t+j) - \bar{I}(u_t, v_t, n) \right)}{\sigma(u_1, v_1, n) \cdot \sigma^*(u_2, v_2, n)} \quad \dots\dots\dots(1)$$

Where u, v are the pixel coordinates; n is the subset size; σ, σ^* are the standard deviations; and I and I^* are the images before and after motion. When the correlation function C is close to one, the subset has been identified in the deformed image. Under real conditions, images contain noise coming from various sources, thus the correlation function will never be a perfect match and interpolation techniques must be used.

For a non-flat specimen, out-of-plane deformations cannot be captured by a single camera setup, thus a configuration with at least two cameras is required to create a 3D point cloud of the specimen. Two cameras in a stereo setup are synchronised by obtaining intrinsic and extrinsic parameters to relate the camera coordinates $x_s(x_s, y_s)$ to the global frame of reference $x_w(x_w, y_w, z_w)$, using a linear pinhole model.

3.3 Experimental Setup

The DIC images were collected and processed using MatchID® software for several fatigue tests at different loading frequencies. The test was performed using three actuators and holding loads for six hours in static before doing 28,000 cycles in fatigue, simulating natural environmental conditions. The DIC setup (Figure 1) consisted of four cameras working in pairs. Two cameras pointed to the region between the root of the blade and the first actuator, and the other two pointed to the region between the first and the second actuator. The loading the blade experienced under the test conditions was a sinusoidal load exerted at 0.7 Hz. The blade was actuated with three separate rams with

equally distributed load between them. During a single loading cycle each actuator exerted the peak load of 65 kN and the minimum load of 15 kN. The blade was subject to one hundred consecutive cycles in a single test.
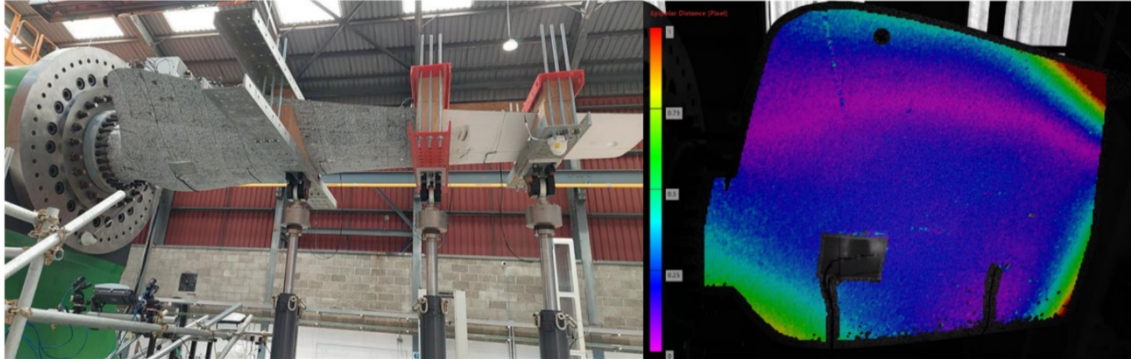
Figure 1. General setup (left-hand). Distortion rate in pixels for a DIC field of view (right-hand).

As a stereo DIC setup is used, calibration is critical to correlate both cameras. 150 high-resolution images were taken targeting a calibration plate with 107 dots evenly spaced by 50 mm. Calibration was done individually for every pair of cameras, and the average error was 0.035845 pixels. As for the fatigue test, another set of images was taken at 7 Hz during the 100 loading cycles with a camera exposure of 12 ms.

Initial pre-processing showed high distortion rates in areas close to the edges, as seen in Figure 1. The field of view in these areas will not give accurate results for displacement and thus, strain. These values were reduced by maximising the area covered by the calibrating plate, resulting in distortions rates greater than one pixel to be isolated to the corners of the blade. Once the images were curated, they were processed to find the displacement field of the region of interest and their corresponding strain values using the criteria shown in Table 1.

Table 1. DIC processing parameters

Subset size	25 [pix]
Step size	10 [pix]
Correlation criterion	Zero-Normalised Mean Sum of Squared Differences [-]
Interpolation function	Local bicubic splines [-]
Shape function	Quadratic [-]
Stereo transformation	Quadratic [-]
Prefiltering	Gaussian [-]
Strain window	15 [-]
Virtual strain gauge	165 [pix]

3.4 Blade Data

The blade (see Figure 1) has a length of 5.25 meters and a weight of 1588.59 kg (15584.07 N). Its natural frequency is approximately 18Hz, and the NACA 63-4XX aerofoil series defines its cross-section. The thickness-to-chord ratio of the blade

decreases from 55% at the root to a minimum of 18% at the tip. The innermost portion of the blade has a cylindrical cross-section with a thickness-to-chord ratio of 100%. This blade is a component of the DeepGen tidal project and was designed by Tidal Generation Limited (TGL) and manufactured by Aviation Enterprises Limited.

4. Data Collection and Pre-Processing

4.1 Original Data

The high-resolution DIC data was collected under the experimental conditions described in *3. Test specification and Set-up*. The dataset collected consists of 97 images representing the maximum strain values for each recorded pixel. The information for each strain reading is stored as a 164 x 288 pixel matrix.

Due to the non-rectangular shape of the area under investigation, non-speckled sections of the specimen, as well as reading errors, each strain map has entries which do not carry any numerical value and are represented as NaN (acronym for *Not a Number*). A sample strain map collected during the test is presented in Figure 2.
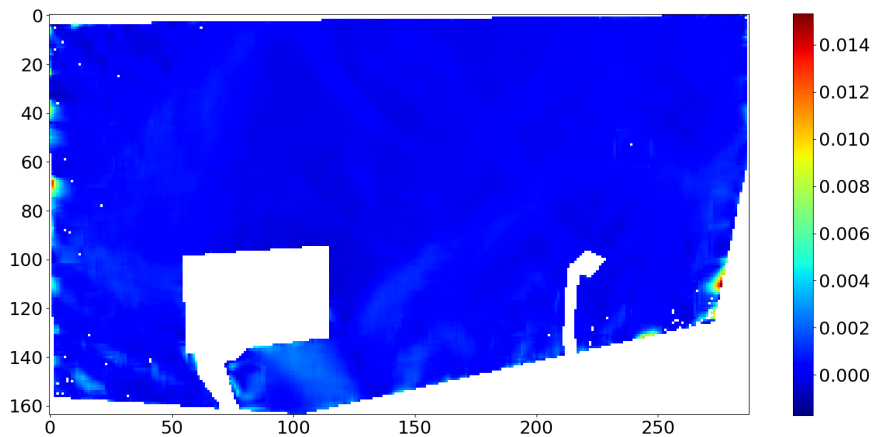

Figure 2. The graphical representation of a randomly chosen image in the dataset collected. Each white pixel represents a NaN entry, whereas other pixels represent local strain measurements. The colour of the pixel is determined by the absolute strain value assigned according to the colour-bar presented.

4.2 Data Mask

Due to the considerations described in *5.1 Tailored Sensing* relating to processing NaNs, each pixel has to be assigned a numerical value. This means, that the cells which carry no numerical values will begin to impact the computational results. The structure of the strain map shows a significant number of single pixels, or small clusters, carrying no numerical value. Each such location was assigned a numerical value as a result of linear interpolation between the adjacent strain readings in a single row.

The manual inspection of the data collected has also revealed an area of the blade where the strain values would consistently deviate from the patterns recorded at the rest of the

blade. The occurrence of the issue is put down to the faulty operation of the DIC software. To mitigate the negative impact of this blade section on the computation of optimal sensor positions and strain map reconstruction, it has also been replaced with NaN values (see Figure 3).
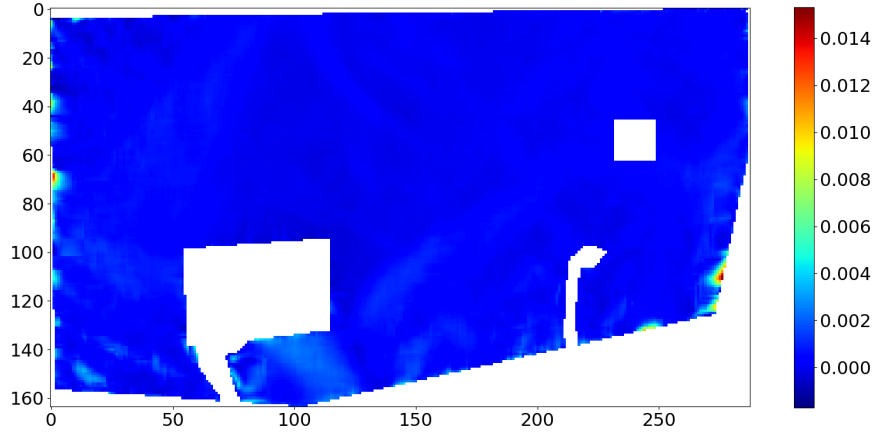
Figure 3. The section of the blade after replacing randomly occurring white pixels with interpolated strain values and cropping the faulty section in the top-right corner of the blade.
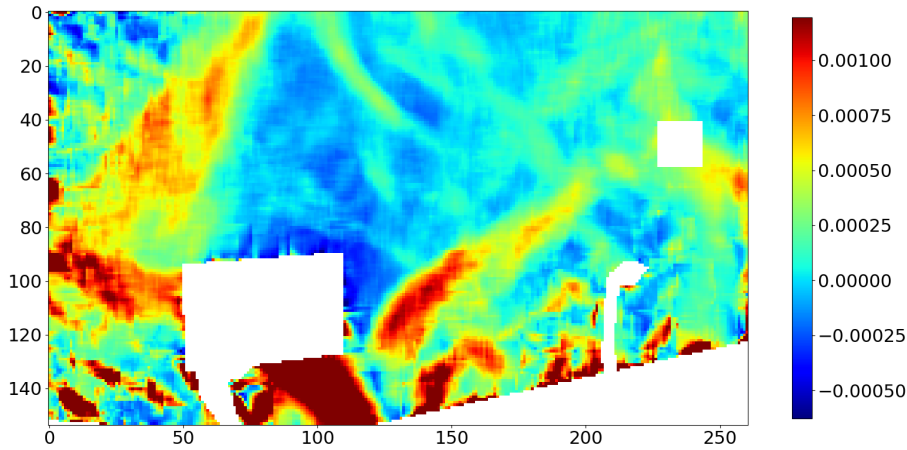
4.3 Contrast Increase

One the problems relating to the quality of the data collected which is evident in Figure 2 and Figure 3 is little variation of the strain values across the plane of the blade, with the only significant hot-spots present at the edges of the structure. The physical interpretation of these results suggests that it is rather unlikely for such desolated high-strain areas to appear in these parts of the blade. Therefore, it is concluded that they result from the imperfection of the DIC software and the values should be amended to enhance the strain contrast in the areas of the blade where high strain is expected.

Anomalies were observed to occur on each edge of the image. Furthermore, the right edge (where the area under test is significantly curved) experiences particularly severe anomalies, which shifts the contrast of the image. As a result, each side of the image was cropped by five pixels, which represents half of the step size used in the DIC data processing (see Table 1). To avoid further problems associated with the unexpected behaviour recorded at the right edge of the investigated area, the image was cropped to the pixel where the transverse curvature of the section begins, by a total of 27 pixels.

To prevent further anomalies from distorting the contrast between different maximum strain patters of the specimen, the range of strain values was limited. The mean, $\bar{x}$, and the standard deviation, σ, for each strain map collected was calculated and the lower and upper boundaries for all possible strain measurements were set to $\bar{x} - 2\sigma$ and $\bar{x} + 2\sigma$ respectively. This way, considering the width of the interval, 4.2% of data was truncated on either side of the distribution. The image which has been subject to the cropping of undesired areas and has had the limited range of strain values applied is presented in Figure 4.

Figure 4. The representation of the cropped strain map with limited range of values. The regions with non-numerical values are represented in white. The resulting increase in the contrast of the strain map can be observed relative to the blade presented in Figure 2 and Figure 3.

Another issue, resulting from the fact that the method for optimising the location of sensors investigated in this work cannot be used on non-numerical values, is the fact that larger areas covered in white (see Figure 4) need to be substituted with auxiliary values. Since all pixels in these sections represent the same type of information (NaN) it was decided that all of them would be assigned the same value. Since a value within the range: $[\,\overline{x} - 2\sigma, \overline{x} + 2\sigma\,]$ would represent a valid strain measurement, the NaN cells are assigned to $\overline{x} - 3\sigma$. Consequently, the non-numerical values never interfere with the strain data but the representation of non-numerical values will differ between each data sample.
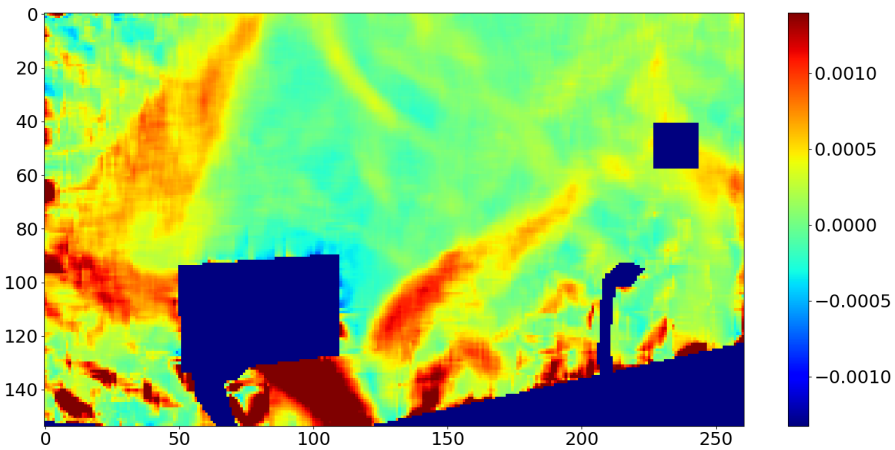
Figure 5. The representation of a single measurement used in the sensor placement optimisation procedure. The treatment of NaNs has decreased the contrast between distinct strain values due to the extension of the strain value range.

5. Sensor Location Optimisation and Data Reconstruction

In this section, the steps taken to compute the optimal sensor placement for reconstructing the high-resolution image of the strain map are presented. The dataset, X,

consists of strain maps, x of dimensions $a \times b$. The strain matrices are flattened into one-dimensional vectors and concatenated so that the dataset has the shape of $(a \cdot b) \times N$, where N is the total number of strain maps.

5.1 Tailored Sensing

The aim of tailored sensing is to reconstruct a high-dimensional signal using low-dimensional measurements of a system. While compressed sensing can be applied to a generic system, tailored sensing targets a system with historic data available. This way, the location of sensors can be tailored to enhance reconstruction results, using as few measuring points as possible. The problem can be presented as [13]:

$$y = C\psi_r a \quad \dots\dots\dots\dots\dots\dots\dots\dots\dots\dots\dots\dots(2)$$

Where y are system measurements at locations given by C, ψ_r is a bases specific to the system considered and a, which is a vector used for image reconstruction, is not sparse as in the case of compressed sensing, but has the same dimensions as y. In tailored sensing the values of C are optimised based on ψ_r. Measuring the values y at the locations defined by C, a can be calculated and subsequently used to reconstruct the high-dimensional image, x.

5.2.1 Dataset-Specific Bases

The bases ψ_r can be constructed from the dataset X using a dimensionality reduction technique. In this work singular value decomposition (SVD) is used to obtain a matrix containing features representative of the entire dataset collected. SVD cannot be applied on matrices with non-numerical values. SVD decomposes a real dataset X into a product of three matrices, U, Σ and V^T. One of the properties of U is that the linear combination of its columns, called singular vectors, can be used to reconstruct any sample x belonging the dataset. Singular vectors represent features which are common for different samples in the dataset, with the first few entries of U storing the highest-level features. Therefore, it is possible to approximate the dataset using just a number of its high-level features, r. Thus [13]:

$$X \cong U_r \Sigma_r V_r^T \quad \dots\dots\dots\dots\dots\dots\dots\dots\dots\dots\dots(3)$$

gives an approximated value of X using first r entries of U, Σ and V^T. U_r, which contains the features common for all samples, has become equivalent to the lower-dimensional approximation of the bases of all strain maps, ψ_r.

5.2.2 Dataset-Specific Bases

The observation made by Manohar et al. [13] is that optimal sensor location can be found when performing pivoted QR factorisation. QR factorisation decomposes a matrix into an orthonormal matrix, Q and an upper triangular matrix R, whereas the process of column pivoting makes some of the QR factorisation instances more efficient. The optimal sensor placement is determined by the location of the pivot points when ψ_r^T undergoes pivoted QR factorisation.

6. Experimental Results

6.1 Sensor Placement Results

The optimisation procedure was carried out on the mean-centred dataset X and the results were validated on a strain map which was not a part of the training dataset. The sensor placement results have been computed for different values of r presented in Figure 6.
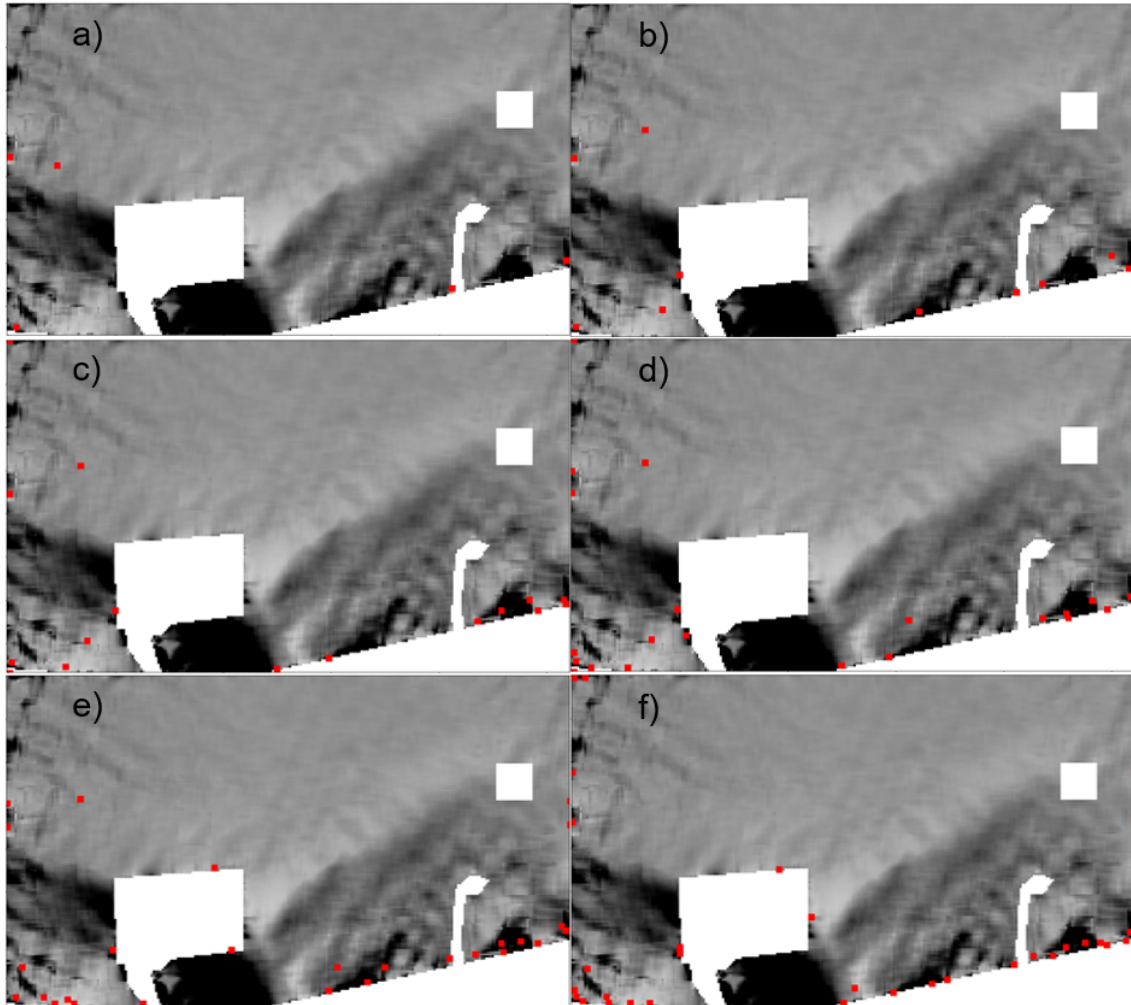

Figure 6. Computed location of sensors (red) presented on a sample strain map. The r values are a) 5, b) 10, c) 15, d) 20, e) 25 and f) 30. Although the location of sensors is given by a unique pixel, they have been visualised with nine pixels.

The experimental results demonstrate clear patterns of how sensors are optimally placed on the blade. It can be noted that sensors tend to be placed at the edges of the blade. Moreover, they also appear in the areas with a high strain gradient, i.e. where the strain values change significantly across a blade small area. This also explains their presence in positions adjacent to the areas which represent the non-numerical values, i.e. along the edges of the blade and the cropped areas within the blade. This implies that these are likely to be the blade areas where the greatest discrepancies between samples occur. It

can also be observed, that sparse sensor placement ($r \leq 10$) is characterised by an even distribution of sensors, while sensor clusters start to appear for denser sensor patterns.

6.2 Reconstruction Results
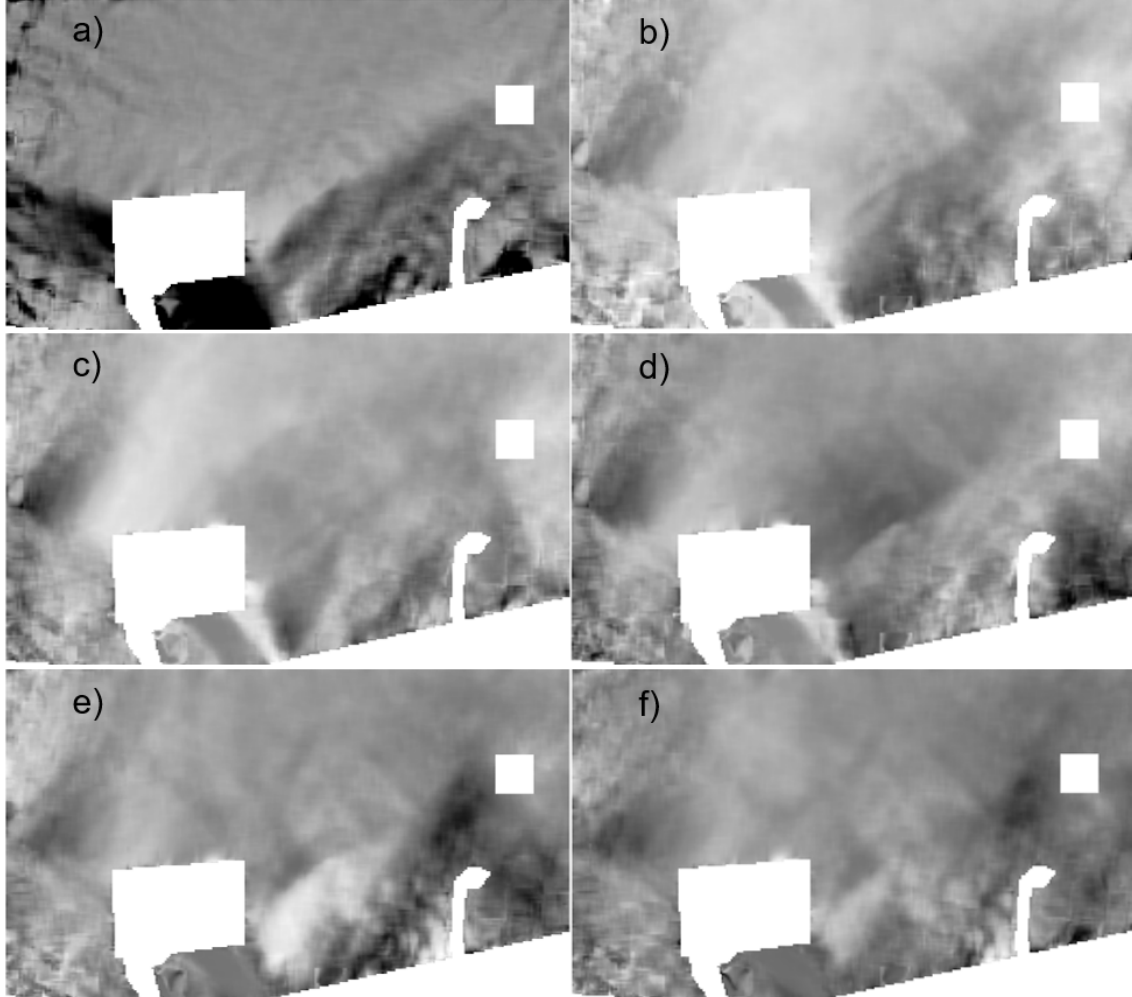
Figure 7. a) is the original image and the reconstructed images are plotted for a sample not belonging to the dataset for the r value of b) 5, c) 10, d) 13, e) 15, f) 20.

Table 2. Reconstruction error values computed for a range of sensor numbers

r	2	5	10	13	15	20
MAE	0.2380	0.1933	0.1691	0.1373	0.1248	0.1083
Relative Error	40.42%	32.83%	28.73%	23.32%	21.20%	18.39%

The mean absolute error (MAE) and relative error for the reconstruction results are presented in Table 2. The visual inspection of images presented in Figure 7 confirms that the maximum strain distribution patterns are preserved across the blade, whereas the contrast of the reconstructed images appears to be different from the original one. The values in Table 2 confirm that the increasing number of sensing points contributes to an increase of the accuracy of the reconstruction. However, the reconstruction error value has shown certain instability when computing values for increasing r, which

might result from the fact that MAE would potentially fail to capture successful pattern reconstruction at a decreased contrast.

7. Conclusions and Further Work

The sensor location has been computed for a range of sensor values. To facilitate recognising patterns of optimal sensor placement, sensor location has also been computed for numbers of strain gauges which would be impractical to install in reality. Several patterns have been identified which will be considered for locating strain gauges on the specimen under test. Their location can be specified by recording a few operational cycles using DIC and identifying areas characterised by a high strain gradient. Moreover, since the areas of sensor congestion were located on the main blade structure (and not in the NaN-dominated regions), the treatment of non-numerical values used in this work seems not to have had a negative impact on optimising sensor locations.

The reconstruction of strain maps consisting of 34,848 strain measurements was successfully demonstrated with fewer than 20 measurements. The patterns of the maximum strain distribution were recreated visually, but the contrast of the reconstructed images was affected. The significant contrast decrease in the pre-processing stage is thought to have affected the reconstruction quality, which suggests that a different NaN value treatment could be considered in the future work.

It is also proposed for the investigation to be repeated on cropped strain maps with solely numerical values. A suggestion for further research is to perform more measurements and investigate the impact of the number of samples in the dataset on the performance of image reconstruction. Performing tests at different cycle frequencies and loading conditions should make the algorithm more robust for future deployment.

References and footnotes

1. D. Song, J.Shen, T. Ma, F. Xu, (2023). Multi-objective acoustic sensor placement optimization for crack detection of compressor blade based on reinforcement learning. Mechanical Systems and Signal Processing, [online] 197, p.110350. doi:https//doi,org/10.1016/j.ymssp.2023.110350.

2. T. Ercan, T. Konstantinos, V. Flores Terrazas, E. Chatzi, and Papadimitriou, (2022). Optimal Sensor Configuration Design for Virtual Sensing in a Wind Turbine Blade Using Information Theory. pp.67-70. Doi://https://doi.org/10.1007/978-3-031-04090-0 8.

3. S. Rucevskis, A. Kovalovs, A. Chate (2023). Optimal Sensor Placement in Composite Circular Cylindrical Shells for Structural Health Monitoring. 2423(1), pp.012021–012021. doi:https://doi.org/10.1088/1742-6596/2423/1/012021.

4. S. Ručevskis, T. Rogala, A. Katunin, (2022). Optimal Sensor Placement for Modal-Based Health Monitoring of a Composite Structure. *Sensors*, 22(10), p.3867. doi:https://doi.org/10.3390/s22103867.

5. Z. Zhang, C. Peng, G. Wang, Z. Ju, L. Ma, (2023). Optimal sensor placement for strain sensing of a beam of high-speed EMU. *Journal of Sound and Vibration*, [online] 542, p.117359. doi:https://doi.org/10.1016/j.jsv.2022.117359.

6. W.-H. Chai, Y.-X. Yang, H. Yu, F.-L. Yang, Z. Yang, (2022). Optimal sensor placement of bridge structure based on sensitivity-effective independence method. 16(2), pp.125–135. doi:https://doi.org/10.1049/cds2.12078.

7. S. Li, A. Coraddu, F. Brennan, (2022). A Framework for Optimal Sensor Placement to Support Structural Health Monitoring. *Journal of Marine Science and Engineering*, [online] 10(12), p.1819. doi:https://doi.org/10.3390/jmse10121819.

8. M. Amer, S. Schmid, M. Paehr, L. Panning-von Scheidt, J.R. Seume, (2012). Optimal Sensor Placement and Model Updating of Axial Compressor Casing Components. pp.1–10. doi:https://doi.org/10.1007/978-3-031-05445-7_1.

9. J.L.J. Pereira, M.B. Francisco, L.A. de Oliveira, J.A.S. Chaves, S.S. Cunha, G.F. Gomes, (2022). Multi-objective sensor placement optimization of helicopter rotor blade based on Feature Selection. *Mechanical Systems and Signal Processing*, [online] 180, p.109466. doi:https://doi.org/10.1016/j.ymssp.2022.109466.

10. G.F. Gomes, F.A. de Almeida, P. da Silva Lopes Alexandrino, S.S. da Cunha, B.S. de Sousa, A.C. Ancelotti, (2018). A multiobjective sensor placement optimization for SHM systems considering Fisher information matrix and mode shape interpolation. *Engineering with Computers*, 35(2), pp.519–535. doi:https://doi.org/10.1007/s00366-018-0613-7.

11. V. Nieminen, J. Sopanen, (2023). Optimal sensor placement of triaxial accelerometers for modal expansion. *Mechanical Systems and Signal Processing*, 184, p.109581. doi:https://doi.org/10.1016/j.ymssp.2022.109581.

12. R. Inoba, K. Uchida, Y. Iwasaki, T. Nagata, Y. Ozawa, Y. Saito, T. Nonomura, K. Asai, (2022). Optimization of sparse sensor placement for estimation of wind direction and surface pressure distribution using time-averaged pressure-sensitive paint data on automobile model. *Journal of Wind Engineering and Industrial Aerodynamics*, [online] 227, p.105043. doi:https://doi.org/10.1016/j.jweia.2022.105043.

13. S.A. Lopez Dubon, and C.R. Vogel, D. García Cava, F. Cuthill, E.D. McCarthy, C.M. Ó Brádaigh, Fastblde: A Technological Facility for Full-Scale Tidal Blade Fatigue Testing. Available at hhttp://dx.doi.org/10.2139/ssrn.4400928

14. K. Manohar, B. W. Brunton, J. N. Kutz, S. L. Brunton, 'Data-Driven Sparse Sensor Placement for Reconstruction: Demonstrating the Benefits of Exploiting Known Patterns', IEEE Control Systems Magazine, vol. 38, no. 3, pp. 63–86, 2018.